

Vortex-Induced Vibration (VIV) hydrokinetic energy harvesting based on nonlinear damping



Baoshou Zhang ^a, Boyang Li ^{b,*}, Song Fu ^a, Zhaoyong Mao ^c, Wenjun Ding ^c

^a School of Aerospace Engineering, Tsinghua University, Beijing, 100084, China

^b College of Electromechanical Engineering, Qingdao University of Science and Technology, Qingdao, Shandong, China

^c School of Marine Science and Technology, Northwestern Polytechnical University, Xi'an, Shaanxi, 710072, China

ARTICLE INFO

Article history:

Received 5 August 2021

Received in revised form

13 May 2022

Accepted 20 June 2022

Available online 25 June 2022

Keywords:

Vortex-induced vibration (VIV)

Ocean current energy

Hydrokinetic energy transfer

Nonlinear damping

Numerical model

ABSTRACT

What is:

1. two way CFD model?
2. non-linear damping?
3. Concave function?

The Vortex-Induced Vibration (VIV) hydrokinetic energy converter can be used to harvest low-speed ocean current energy. In order to match the nonlinear resonance response in VIV, the nonlinear damping model is proposed. A two-way CFD numerical model is developed to simulate the VIV responses. The nonlinear damping model ($C_t = C_{max}(V_t/V_{max})^n$) contains two control parameters: C_{max} is the maximum preset damping; n is the model exponent. In the nonlinear damping model, when the vibration velocity is low, small damping is adopted to reduce resistance for VIV; when the vibration velocity is high, large damping is adopted to enhance energy transfer performance. It can be found that nonlinear damping is more efficient than constant damping, thereby improving the adaptability of the converter. Besides, the optimal nonlinear damping model belongs to a concave function. For the concave function model, the damping changes sensitively when the vibration velocity is high; when the vibration velocity is low, the damping remains stable. The effects of the model parameters on the VIV response and converted power are nonlinear, so a ridge-shaped fitted response surface of the vibration power is observed. Finally, after introducing nonlinear damping, the vibration power is significantly improved when compared to the optimal constant damping.

© 2022 Elsevier Ltd. All rights reserved.

1. Introduction

Vortex-Induced Vibration (VIV) may occur on an elastically mounted cylinder in a flow. More specifically, a series of vortices are generated on both sides of the cylinder and provide periodic lift resulting in VIV. As yet, the VIV responses have been studied extensively. Bearman [1] studied the vortex shedding from oscillating cylinders. Khalak et al. [2] and Williamson et al. [3] found initial branch, upper branch and lower branch of the VIV amplitude. The effects of system parameters such as damping and stiffness, etc. on the VIV response have also been analyzed. Lee et al. [4] studied the effect of stiffness using virtual spring system on VIV. Klamo et al. [5] found high damping will change the characteristics of the VIV amplitude. Only two branches (Initial branch and Lower branch) are observed when at high damping. In recent years, the studies on VIV focused on vortex shedding mode [6,7], VIV suppression [8–10] and multi-body interaction [11,12].

VIV is a strong Fluid-structure interaction (FSI) resonance. Therefore, the oscillator in VIV can be used as a powerful mechanism for transferring hydrokinetic energy from ocean currents to the oscillator [13]. Based on the mechanism mentioned above, Bernitsas et al. [14,15] first introduced the VIV hydrokinetic energy harvesting system, which is named as VIVACE (VIV for Aquatic Clean Energy) converter. The VIV hydrokinetic energy converter can be modelled as shown in Fig. 1(a). The oscillator (cylinder) in VIV drives the generator through transmission mechanisms to generate electricity. The converter shows promise as a successful commercial device and has been discussed in more detail in articles [16–18]. Notably, the VIVACE converter built in the MRELab at the University of Michigan has been successfully tested in a river [19], as shown in Fig. 1(b). In order to enhance the energy harvesting performance, the system parameters of the converter are extensively optimized experimentally [11,20–22]; and numerically [23–25]. The VIV hydrokinetic energy converter can extract energy from flows as slow as 0.27–0.4 m/s and with no upper limit [26,27]. Moreover, based on similar mechanism, Wang et al. [28,29] studied VIV energy harvesting using metasurface from wind. Zhu et al. [30] and Zhang et al. [31,32] studied VIV energy harvesting using non-

* Corresponding author.

E-mail address: qdlby@126.com (B. Li).

Nomenclature

A	m VIV amplitude
$A^* = A/D$	– Amplitude ratio
C	N/(m/s) Damping
C_t	N/(m/s) Current damping
C_{max}	N/(m/s) Maximum upper limit of damping
D	m Diameter of cylinder
f_{VIV}	Hz VIV frequency
$f_{n,water} = (1/2\pi)\sqrt{K/(M)}$	Hz Cylinder's natural frequency
$f_{fluid,y}(t)$	N Fluid force
K	N/m Spring stiffness
L	m Length of rectangular cylinder
M_{total}	kg Total vibration mass
m_{add}	kg Added mass

m_{disp}	kg Displaced fluid mass
$m^* = M_{total}/m_{disp}$	– Mass-ratio
n	– Model exponent
P_{VIV}	W Converter power in VIV
P_{fluid}	W Power input from the fluid
$Re = UD/v$	– Reynolds number
T_{VIV}	s Period of vibration
U	m/s Flow velocity
v	(m^2)/s Kinematic viscosity
V_t	m/s Current vibration velocity
V_{max}	m/s Maximum vibration velocity
$U^* = U/(f_{n,water} \cdot D)$	– Reduced velocity
$\xi = C/(2\sqrt{(M) \cdot K})$	– Damping ratio
η_{VIV}	– Energy transfer efficiency

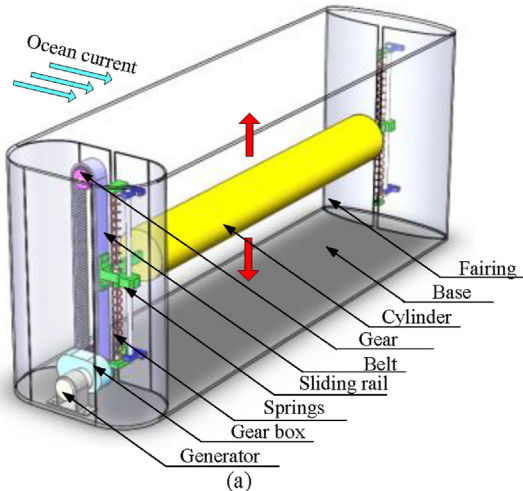


Fig. 1. (a) VIV hydrokinetic energy converter [17] and (c) VIVACE converter built in the MRELab [19].

circular cross section oscillators. Mehmood et al. [33] numerically studied VIV energy harvesting based on a piezoelectric transducer.

In past studies, since the effective VIV converted power is from load damping, it is essential to study the effects of damping on VIV. Raghavan et al. [34] studied the effect of damping on VIV energy harvesting and found high damping is required to achieve high power output. Soti et al. [35,36] found the optimal damping ratio at which the power is maximum is about 0.074–0.095. Lee et al. [37] reported the optimal value of damping ratio exists and the optimal damping ratio is 0.12. Indeed, due to the common influence of multiple system parameters, researchers have not reached a consensus on the optimal damping. Sun and Kim et al. [26,38] reported the highest converted power is obtained when the damping ratio is 0.20–0.24. In summary, if small damping is used, VIV amplitude is high, but the converted power is relatively low. On the contrary, if large damping is adopted, VIV response is always suppressed, which would in turn lead to a further reduction of effective power. As a result, the constant damping is not the best choice for the VIV energy harvesting system, since the vibration velocity is nonlinear.

Therefore, the nonlinear damping scheme becomes an inevitable consequence for the VIV energy harvesting system. In particular, the nonlinear damping oscillator will not be restricted by

constant damping due the dynamic change of damping with respect to the vibration velocity. However, up to now only few studies focused on nonlinear damping. It is noteworthy that Li et al. [39] reported a novel energy-harvesting variable damping for electric vehicles and found higher efficiency (35.24%) can be achieved. Similarly, inspired by the trout, Sun and Bernitsas [40] proposed a bio-inspired adaptive damping for the VIV energy conversion system (Fig. 2). In a word, the influence of nonlinear damping has been studied but still is not well understood for VIV hydrokinetic energy harvesting.

Nonlinear damping is a potential scheme for improving the energy harvesting performance of the VIV system. In this study, the VIV hydrokinetic energy converter with nonlinear damping is studied numerically. The nonlinear damping model ($C_t = C_{max}(V_t/V_{max})^n$) belongs to power function model, in which the damping increases nonlinearly with the vibration velocity. C_{max} is the maximum preset upper limit of damping; n is the model exponent. Simulations are conducted in the range of $20 \leq C_{max} \leq 100$ and $0.5 \leq n \leq 30$ to cover the effective damping region. In Section 1, an overview of literature about the VIV energy harvesting and the effects of damping on VIV are introduced. In Section 2, the physical model of the VIV energy converter and nonlinear damping model are introduced. The mathematical model of energy transfer and FSI

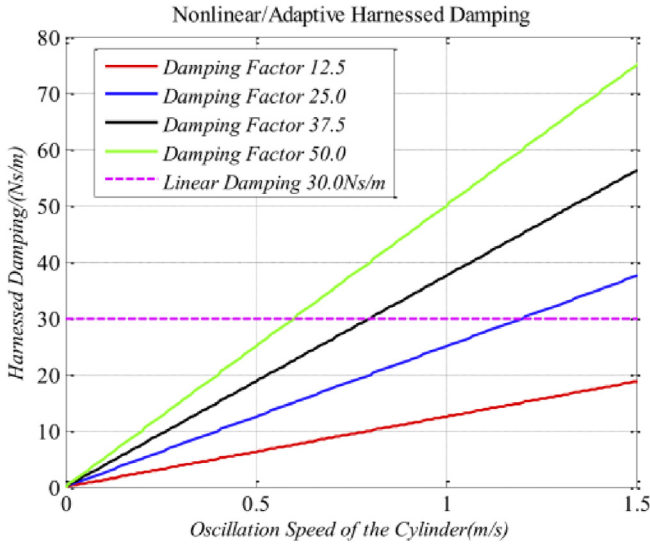


Fig. 2. Adaptive harnessing damping reported by Sun et al. [40].

simulation method are given in Section 3. In Section 4, VIV responses with different damping models are analyzed and compared in detail. In Section 5, the VIV amplitude and frequency responses, converted power and efficiency with different damping models are discussed. Conclusions are summarized at the end.

2. Geometry configuration

2.1. Physical model

In this work, the simplest schematic of the VIV hydrokinetic energy converter is shown in Fig. 3, which consists of a circular cylinder suspended by springs, transmission mechanisms and a generator. This cylinder with one degree-of-freedom is the oscillator of the VIV energy harvesting system. According to previous study [18,19], the main parameters of the VIV hydrokinetic energy converter are determined and listed in Table 1. It is well-known that energy is extracted as the byproduct of damping. The effect of nonlinear damping is studied numerically. The total damping comes from the Power-Take-Off system (including transmission mechanisms and the generator).

The initial constant damping ratio ξ of the VIV system is set to 0.1, so the damping C is about 24N/(m/s). By the way, the relationship between the damping C and damping ratio is defined as: $C = 2\xi\sqrt{K(M)}$. If the effect of added mass is considered together

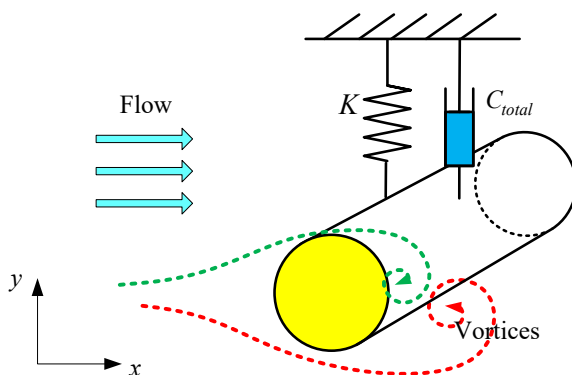


Fig. 3. Schematic of the VIV hydrokinetic energy converter.

Table 1
Parameters of the VIV hydrokinetic energy converter.

Description	Symbol	Value
Total vibration mass	M_{total} (kg)	13.63
Added mass	m_{add} (kg)	7.9
Mass ratio	m^*	1.725
Diameter of cylinder	D (m)	0.089 (3.5inch)
Length of cylinder	L (m)	1.0
Damping ratio	ξ	0.1
Effective damping	C (N/(m/s))	24
Spring stiffness per unit length	K (N·m)	1063
Natural frequency in water	$f_{n,water}$ (Hz)	1.12

(i.e. $M = M_{total} + m_{add}$), the total damping including additional damping is about 30N/(m/s). The additional damping produced by the added mass (or the additional inertial force) does not generate effective power, so the additional damping is not considered in this study.

Overall, the optimal damping is a research hotspot. Relatively high damping is always used to enhance energy transfer performance, and also leads to suppression of VIV. In previous studies about VIV energy harvesting, because of the difference of the experimental setup, there is no consensus on the optimal damping. In this work, the effect of constant damping ($0.02 < \xi < 0.3$; $4.81 < C < 72.24$) on converted power is studied first. Finally, the optimal constant damping is regarded as the comparative reference group. According to the numerical results, the constant damping and converted power are listed and compared in Table 2.

The power of the converter under different damping ratios is presented in Fig. 4. When the damping ratio changes from 0.02 to 0.15, the converted power increases from 1.105W to 3.626W. When the damping ratio is larger than 0.15, the converted power starts to decrease. Therefore, the optimal damping ratio is 0.15 for the current VIV energy harvesting system. In the following studies, the case of $\xi = 0.15$ will be used as a comparative reference group.

2.2. Nonlinear damping model

In the VIV response, the vibration velocity of the cylinder changes alternately. The basic idea of nonlinear damping is the damping changes with the vibration velocity, which is also known as "velocity-proportional damping". When the vibration velocity is low, small damping is adopted. Therefore, the converter will not be restricted. When the vibration velocity is high, large damping is adopted, so the converted power will be further enhanced. The nonlinear damping model is established as:

$$C_t = C_{max}(V_t/V_{max})^n \quad (1)$$

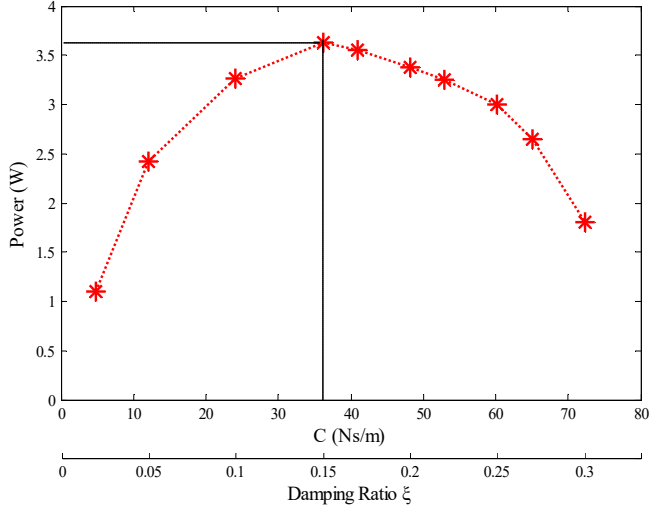
where C_t is the damping at the current moment. C_{max} is the maximum preset upper limit of damping. n is the model exponent, which controls the sensitivity of the nonlinear damping model. For instance, when n is relatively large, the damping increases sharply in the high-speed vibration range. V_t is the vibration velocity. V_{max} is the recorded maximum vibration velocity. V_t/V_{max} is the vibration velocity ratio. The C_t/C_{max} Vs V_t/V_{max} curves under different exponent n are compared in Fig. 5. As expected, as the exponent n increases from 1/5 to 30, the damping becomes more sensitive when in the high-speed vibration range.

By the way, a conceptual discussion on how to physically incorporate the non-linear damping mechanism into the VIV system is also given. In general, the nonlinear damping mechanism is achieved by using the variable load resistance which is connected to a generator. Firstly, according to the vibration velocity and nonlinear damping model, the computer outputs signals to the

Table 2

Constant damping and converted power.

Damping Ratio ξ	0.02	0.05	0.1	0.15	0.17	0.2	0.22	0.25	0.27	0.3
Damping C	4.816	12.039	24.079	36.118	40.934	48.157	52.973	60.197	65.012	72.236
Converted Power	1.105	2.4276	3.264	3.626	3.550	3.383	3.245	3.002	2.644	1.808

**Fig. 4.** The power of the converter under different constant damping ratios.

resistance controller. Then, the resistance controller adjusts the variable load resistance. Therefore, after changing the resistance, the total damping of the system can be changed.

In order to cover the effective damping as much as possible, 40 damping models with different parameters are studied in detail in the following sections. The 40 damping models are listed in **Table 3**.

3. Numerical simulation

3.1. Mathematical model of power and efficiency

The VIV hydrokinetic energy converter belongs to the mass-spring-damper oscillator model. The mathematical model for the VIV system is presented in this section. The cylinder is allowed to move freely in the y -direction. A second-order linear differential equation can be used to model the response of the cylinder in VIV:

$$M\ddot{y} + C_t\dot{y} + Ky = F_{fluid,y}(t) \quad (2)$$

where M is the total vibration mass; and $F_{fluid,y}(t)$ represents the total fluid force acting on the cylinder in y direction.

The converted power P_{VIV} of the cylinder in one cycle T_{VIV} is calculated by:

$$P_{VIV} = \frac{1}{T_{VIV}} \int_0^{T_{VIV}} (M\ddot{y} + C_t\dot{y} + Ky)\dot{y} dt \quad (3)$$

According to previous studies [18,19], the $M\ddot{y}$ and Ky terms are two zero terms. As a result, only the $C_t\dot{y}$ term is a nonzero term. Therefore, we have:

$$P_{VIV} = \frac{1}{T_{VIV}} \int_0^{T_{VIV}} C_t\dot{y}^2 dt \quad (4)$$

In the simulation process, the velocity \dot{y} can be obtained

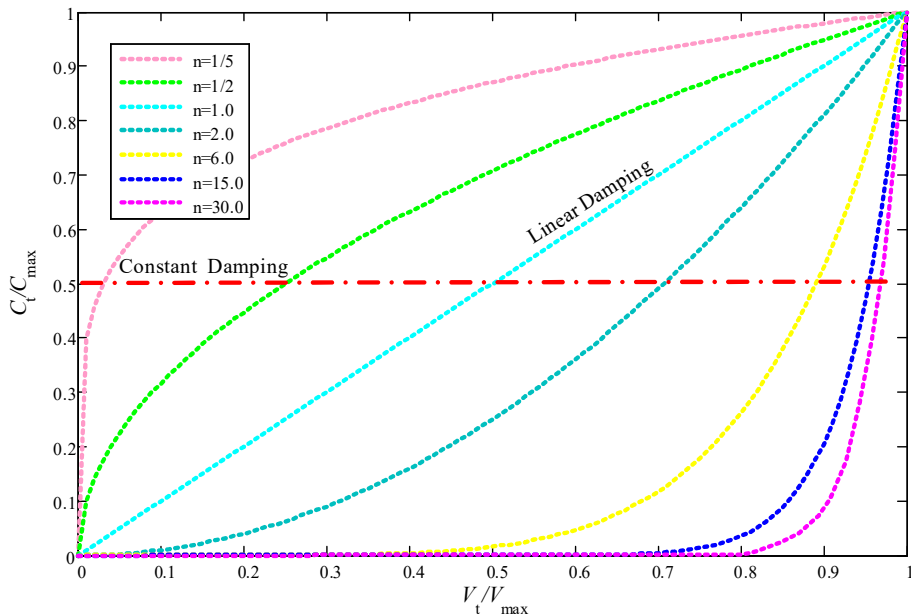
**Fig. 5.** Comparison between constant damping, linear damping and 6 different nonlinear damping models with the exponent $n = 0.2, 0.5, 1, 2, 6, 15, 30$

Table 3

Forty damping models with different parameters.

C_{max} n	0.5	1	2	4
20	$C_t = 20(V_t/V_{max})^{0.5}$	$C_t = 20(V_t/V_{max})^{1.0}$	$C_t = 20(V_t/V_{max})^{2.0}$	$C_t = 20(V_t/V_{max})^{4.0}$
40	$C_t = 40(V_t/V_{max})^{0.5}$	$C_t = 40(V_t/V_{max})^{1.0}$	$C_t = 40(V_t/V_{max})^{2.0}$	$C_t = 40(V_t/V_{max})^{4.0}$
60	$C_t = 60(V_t/V_{max})^{0.5}$	$C_t = 60(V_t/V_{max})^{1.0}$	$C_t = 60(V_t/V_{max})^{2.0}$	$C_t = 60(V_t/V_{max})^{4.0}$
80	$C_t = 80(V_t/V_{max})^{0.5}$	$C_t = 80(V_t/V_{max})^{1.0}$	$C_t = 80(V_t/V_{max})^{2.0}$	$C_t = 80(V_t/V_{max})^{4.0}$
100	$C_t = 100(V_t/V_{max})^{0.5}$	$C_t = 100(V_t/V_{max})^{1.0}$	$C_t = 100(V_t/V_{max})^{2.0}$	$C_t = 100(V_t/V_{max})^{4.0}$
C_{max} n	6	10	15	30
20	$C_t = 20(V_t/V_{max})^{6.0}$	$C_t = 20(V_t/V_{max})^{10}$	$C_t = 20(V_t/V_{max})^{15}$	$C_t = 20(V_t/V_{max})^{30}$
40	$C_t = 40(V_t/V_{max})^{6.0}$	$C_t = 40(V_t/V_{max})^{10}$	$C_t = 40(V_t/V_{max})^{15}$	$C_t = 40(V_t/V_{max})^{30}$
60	$C_t = 60(V_t/V_{max})^{6.0}$	$C_t = 60(V_t/V_{max})^{10}$	$C_t = 60(V_t/V_{max})^{15}$	$C_t = 60(V_t/V_{max})^{30}$
80	$C_t = 80(V_t/V_{max})^{6.0}$	$C_t = 80(V_t/V_{max})^{10}$	$C_t = 80(V_t/V_{max})^{15}$	$C_t = 80(V_t/V_{max})^{30}$
100	$C_t = 100(V_t/V_{max})^{6.0}$	$C_t = 100(V_t/V_{max})^{10}$	$C_t = 100(V_t/V_{max})^{15}$	$C_t = 100(V_t/V_{max})^{30}$

numerically. Therefore, Eq. (4) is adopted to calculate the converted power.

The input power of fluid over the area swept by the cylinder can be calculated by:

$$P_{fluid} = 0.5\rho U^3 L(D + 2A) \quad (5)$$

where U is the flow velocity. L is the length of cylinder; D is the diameter of cylinder. A is the amplitude of VIV.

Energy transfer efficiency is another key parameter of the VIV energy system. The energy transfer efficiency η_{VIV} is calculated by:

$$\eta_{VIV} = \frac{P_{VIV}}{P_{fluid} \times \text{Betz Limit}} \times 100\% \quad (6)$$

where $\text{Betz Limit} = 16/27$ (0.593) represents the maximum efficiency that can be extracted from flow, which is widely used to assess the energy transfer efficiency [19,41].

3.2. FSI simulation method

VIV is a typical FSI (Fluid-Structure Interaction) response. In this study, the numerical simulation process for VIV consists of two parts: solving the fluid force and solving the motion. Since the current study focuses on the effect of nonlinear damping, the governing equations and computational domain etc. are not given in this paper, which have been discussed in detail in previous studies [16–18]. The flowchart of the simulation process is given in Fig. 6. The numerical method is briefly introduced as follows:

- (1) According to the current vibration velocity V_t , the damping C_t is obtained based on the nonlinear damping model (Eq. (1)), which will be used in the following steps.
- (2) Obtaining fluid force is the basis of motion simulation. Specifically, CFD software Fluent using the RANS (Reynolds-Averaged Navier–Stokes) equations with the SST $k-\omega$ model is adopted in this study.
- (3) UDF (User-Defined Functions) module is used to complete the two-way communication between the fluid force and the motion. The second-order linear differential equation (Eq. (2)) is solved based on Newmark- β method. The developed computer algorithms of Newmark- β method have been embedded in UDF. Therefore, the vibration velocity V_t , displacement, etc. could be obtained.

In order to verify the numerical model in this study, the numerical results have been compared with other experimental and numerical results, such as Jauvtis and Williamson [42] and Kang

et al. [43], etc, as shown in Fig. 7. VIV system parameters for numerical method validation have been reported by other member of our research group [44], in which we used similar numerical simulation methods. Three branches (initial branch, upper branch, and lower branch) are all observed. Therefore, the numerical method is acceptable.

4. VIV responses with different damping models

To analyze the effect of nonlinear damping quantitatively, the results of VIV responses and flow structures under different damping models are discussed. A linear damping model and two nonlinear damping models (Concave function model and Convex function model) are compared with the optimal constant damping model in this section. In general, increasing exponent n has a positive impact on the VIV response, especially when the maximum damping C_{max} is higher than 40 N/(m/s). However, the effects of the model parameter C_{max} on the VIV response and converted power are nonlinear. When C_{max} is relatively low, the power decreases with the exponent n ; when C_{max} is relatively high, the converted power increases with the exponent n .

4.1. Linear damping and constant damping

The linear damping model $C_t = 60(V_t/V_{max})^{1.0}$ and the optimal constant damping model $C = 36.12\text{N}/(\text{m/s})$ ($\xi = 0.15$) are compared in Fig. 8. The flow velocity is 0.55 m/s (The reduced velocity U^* is about 6), which is located in the VIV upper branch. For the linear damping model, the damping increases linearly with vibration velocity. When $V_t/V_{max} < 0.602$, the linear damping C_t is less than the constant damping ($C = 36.12\text{N}/(\text{m/s})$). As the vibration velocity ratio V_t/V_{max} increases, the linear damping C_t is higher than the constant damping and keeps growing until the maximum upper limit of damping $C_{max} = 60\text{N}/(\text{m/s})$ is achieved.

The time history of the fluid force, vibration velocity, displacement, damping, and converted power of the linear damping model are compared with the constant damping model, as shown in Fig. 9. In the first 8 s, the damping is irregular since the recorded maximum vibration velocity V_{max} is still increasing. Then, the damping changes regularly. The VIV responses of the linear damping oscillator is slightly weaker than the optimal constant damping oscillator (see Fig. 9). It can be observed that the maximum fluid force of the linear damping oscillator is 20.5N. The maximum fluid force of the optimal constant damping is 27.3N, which is higher than linear damping (33% higher). The maximum vibration velocity of the linear damping is 0.41 m/s. The maximum vibration velocity of the constant damping is about 0.49 m/s (19.5% higher), which is

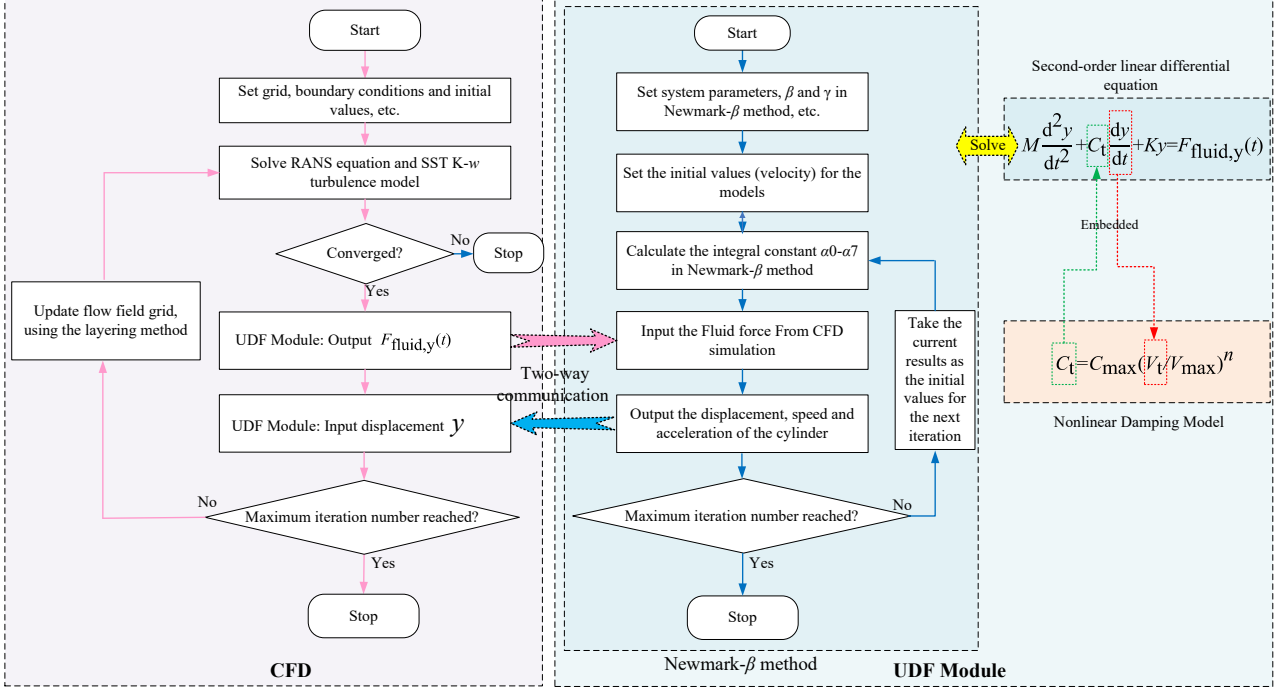


Fig. 6. Numerical simulation process of the VIV responses with nonlinear damping model.

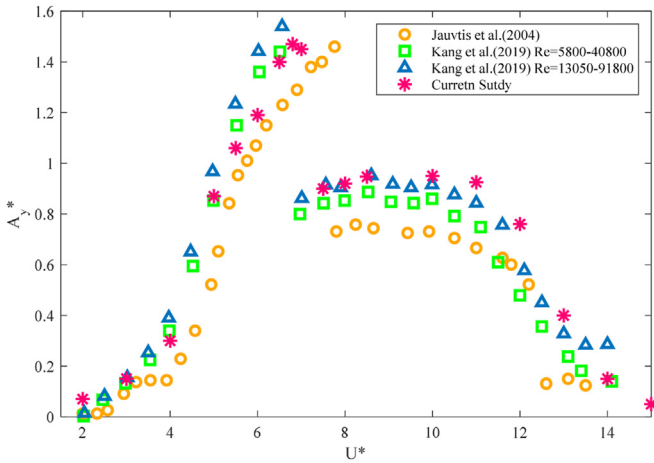


Fig. 7. Comparison of the numerical results with other results from Jauvtis et al. [42] and Kang et al. [43].

higher than the linear damping. Similar results are found when analyzing the maximum amplitude of displacement ($0.0488\text{m} < 0.07\text{m}$). The effects of damping on the VIV frequency are weak, since the VIV frequency is closely related to the stiffness, mass and vortex shedding frequency. Therefore, the frequency of the linear damping oscillator is 1.18Hz, which is close to the constant damping (1.16Hz).

The average damping of the linear damping is $30\text{N}/(\text{m/s})$, which accounts for 83.33% of the optimal constant damping $C = 36\text{N}/(\text{m/s})$. However, the converted power of the linear damping (3.351W) is much closer to the power of the constant damping (3.626W). In other words, although the average damping of the linear damping accounts for 83.33% of the optimal constant damping, the converted power of the linear damping accounts for 92.42% of the optimal constant damping, which means the variable damping is

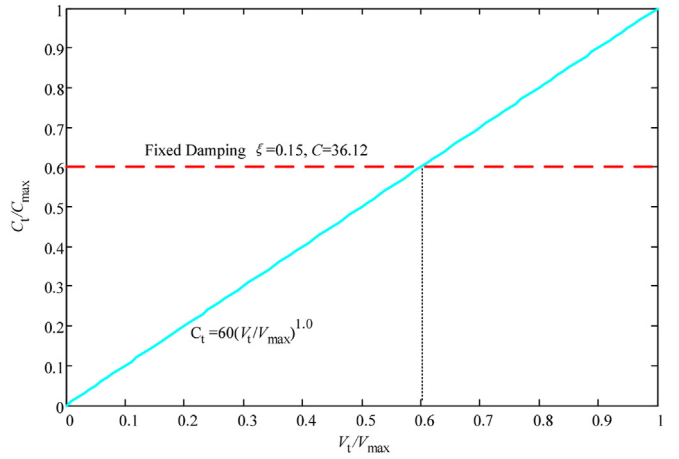


Fig. 8. Comparison between the constant damping model and linear damping model.

more suitable for the change of velocity.

In order to better explain the VIV response, the velocity distribution and wake vortex structure for the oscillators with different damping models are compared in Fig. 10 and Fig. 11. In Fig. 10, two rows of vortices are parallel and rotate in opposite directions. This phenomenon is similar to the classical von Kármán vortex street. The distance H between two rows of vortices is close to 0.2m because of the relatively large amplitude ($A = 0.07\text{m}$, $A^* = A/D = 0.79$). It is found that two single vortices are shed from the cylinder in one cycle. Therefore, the vortex pattern is named 2S (S, Single).

Generally speaking, the VIV amplitude and flow velocity affect the vortex shedding mode together. For a VIV system with low damping ratio (especially damping ratio <0.1), there will be 3 branches (initial branch, upper branch, and lower branch). In the VIV upper branch, the VIV amplitude is the highest, and the

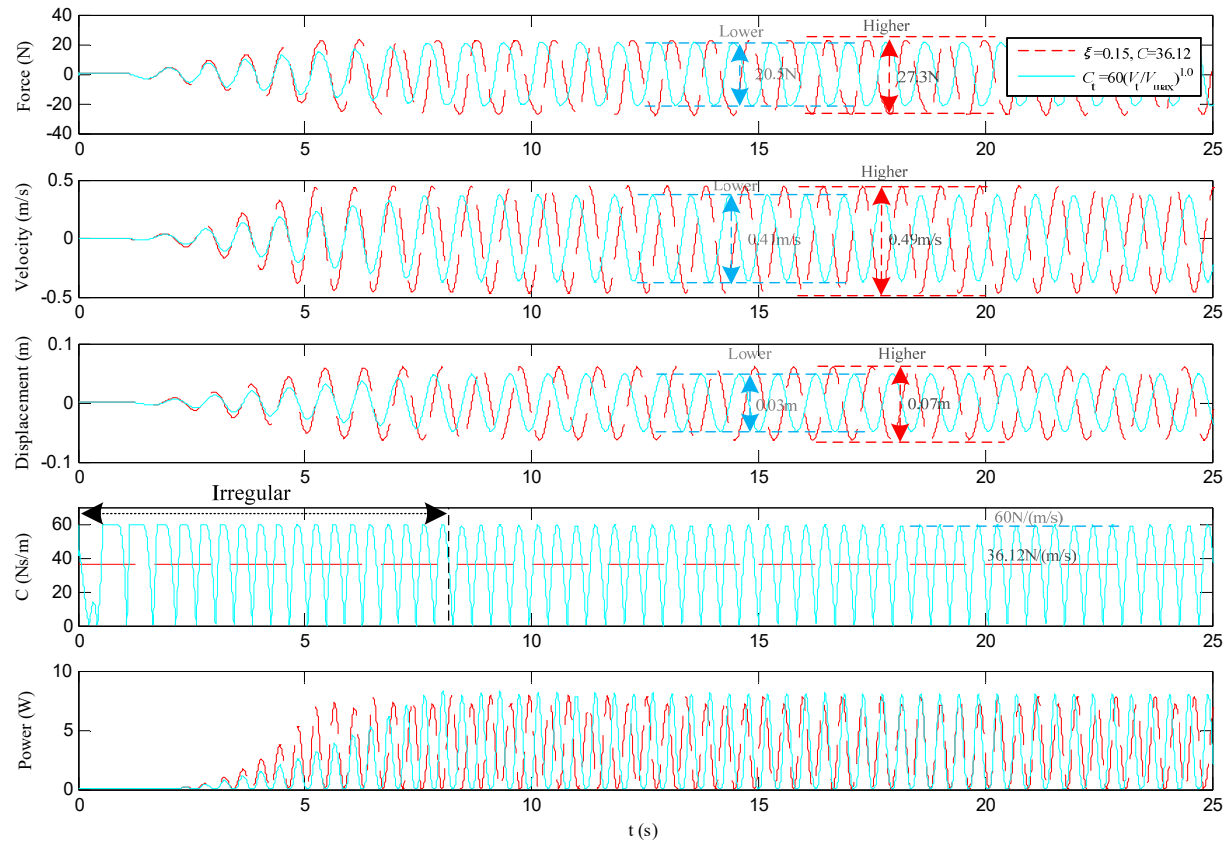


Fig. 9. Comparison of the fluid force, vibration velocity, displacement, damping, and converted power with the linear damping model to the constant damping model.

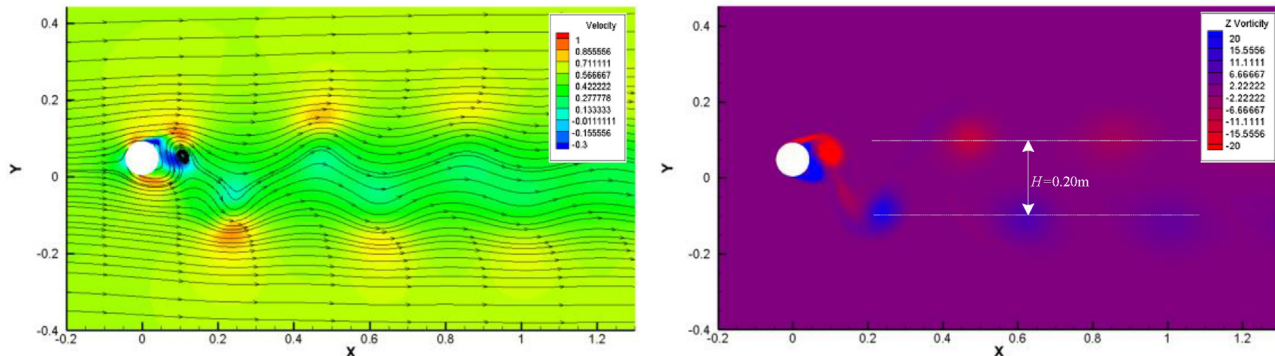


Fig. 10. Velocity distribution and Vortex pattern around the cylinder with the constant damping.

amplitude ratio exceeds 1.0 or even reaches 1.4–1.5, so the vortices have enough space to generate and develop. Therefore, the vortex shedding mode in the VIV upper branch is 2P ($P = \text{pair}$) pattern. However, in this study, the damping is relatively high. For example, the optimal constant damping ratio is 0.15. In this case, the VIV amplitude is relatively low, so there is not enough space for vortex generation, which causes 2P pattern is not significant. Instead, 2S pattern become more obvious, as shown in Figs. 10 and 11. In a word, the vortex shedding mode is related to VIV amplitude and flow velocity.

In Fig. 11, since the amplitude of the linear damping oscillator ($A = 0.048\text{m}$, $A^* = 0.55$) is lower than the constant damping oscillator ($A = 0.07\text{m}$, $A^* = 0.79$), the distance H (0.17m) between two rows of vortices is also relatively small.

4.2. Nonlinear damping (concave function model)

When the exponent n is less than 1, the nonlinear damping model $C_t = C_{\max}(V_t/V_{\max})^n$ is a concave function. The nonlinear damping model $C_t = 80(V_t/V_{\max})^{0.5}$ is selected as an example and compared with the optimal constant damping model, as shown in Fig. 12. Half of the maximum preset upper limit of damping is 40N/(m/s), which is higher the constant damping (36.12N/(m/s)). In the concave function model, the damping changes rapidly when V_t/V_{\max} is relatively low. As the vibration velocity ratio V_t/V_{\max} increases, the growth rate of the damping gradually decreases. Therefore, the damping changes slowly when the vibration velocity ratio V_t/V_{\max} is relatively high.

The comparison of fluid force, vibration velocity, displacement,

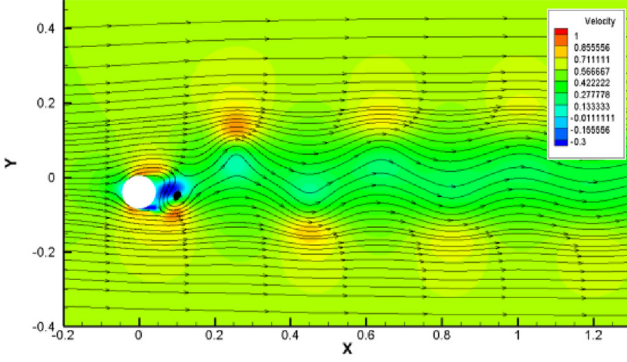


Fig. 11. Velocity distribution and Vortex pattern around the cylinder with the linear damping $C_t = 60(V_t/V_{max})^{1.0}$

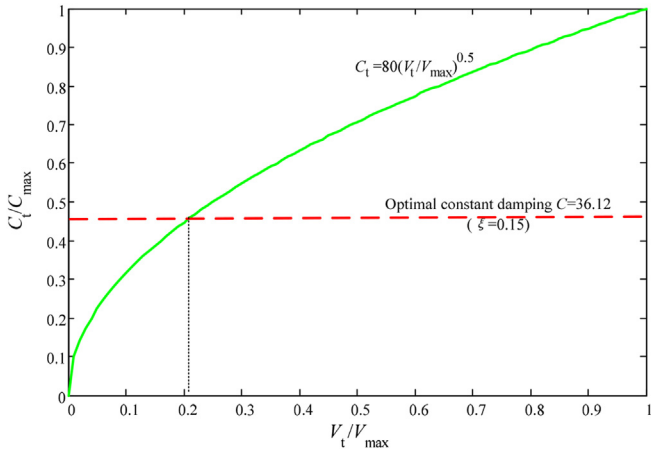
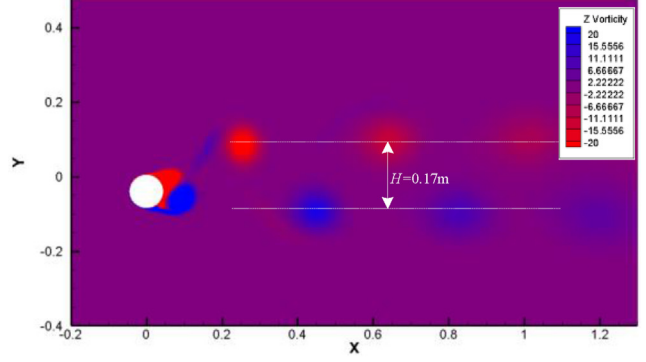


Fig. 12. Comparison between the constant damping model and nonlinear damping model $C_t = 80(V_t/V_{max})^{0.5}$ (Concave Function Model).

damping, and power between the nonlinear damping model $C_t = 80(V_t/V_{max})^{0.5}$ and constant damping model is presented in Fig. 13. In the first 8 s, the change of the nonlinear damping is irregular since the maximum vibration velocity V_{max} is unstable. After 8 s, the VIV responses change regularly in different cycles. The nonlinear damping value is higher than the constant damping value in most cases, which suggests the VIV responses with the nonlinear damping model are suppressed. The maximum amplitude of the nonlinear damping is only 0.03 m (42.9% of the constant damping). The maximum fluid force of the nonlinear damping oscillator (17 N) is lower than the constant damping oscillator (27.3 N). Besides, the maximum vibration velocity with the nonlinear damping model is 0.24 m/s that only accounts for 49% of the constant damping oscillator (0.49 m/s). The converted power is very sensitive to the vibration velocity, because the power is proportional to the square of vibration velocity (y). Consequently, the average power of the nonlinear damping oscillator is significantly lower than the constant damping oscillator (1.4731 W < 3.626 W).

The velocity distribution and vortex pattern around the cylinder with the nonlinear damping model are given in Fig. 14. Because of the relatively low amplitude ($A = 0.03$ m, $A^* = A/D = 0.34$), the distance H between two rows of vortices is only 0.085 m, which is lower than the constant damping oscillator. The vortex pattern is also 2S pattern. The velocity in the wake is much lower. Besides, the velocity in the wake is relatively lower, while the velocity far from the wake is relatively higher. The reason is that on the outside of the



wake, the rotation direction of the vortex is the same as the flow direction, resulting in higher velocity.

4.3. Nonlinear damping (convex function model)

When the exponent n is higher than 1, the nonlinear damping model is a convex function. $C_t = 80(V_t/V_{max})^{15}$ is selected as an example in this section (Fig. 15). In the convex function model, the damping is close to zero when the vibration velocity ratio V_t/V_{max} is relatively low. As the vibration velocity ratio V_t/V_{max} increases, the damping increases rapidly, especially when V_t/V_{max} exceeds 0.7. When V_t/V_{max} exceeds 0.93, the nonlinear damping is higher than the optimal constant damping. Therefore, the damping of the nonlinear damping model $C_t = 80(V_t/V_{max})^{15}$ is less than the optimal constant damping model in most cases.

The time history of the fluid force and vibration velocity, etc. of the nonlinear damping is compared with the optimal constant damping in Fig. 16. In the first 10 s, the damping is still changing irregularly. After 10 s, the damping changes regularly. Half of the maximum preset upper limit of damping 80 N/(m/s) is 40 N/(m/s) and higher than the constant damping 36.12 N/(m/s). For the nonlinear damping oscillator, a significant drop is observed in the peak of the fluid force in each cycle. However, the fluid force acting on the constant damping oscillator is close to simple harmonic response. According to the nonlinear damping model $C_t = 80(V_t/V_{max})^{15}$, the exponent n is 15, which means the damping changes sharply when the vibration velocity is relatively high. Therefore, when V_t approaches V_{max} , high damping will be introduced quickly. This directly leads to the drops of fluid force in the peak. Moreover, the drops also indirectly change the rate of change of velocity and displacement. Thus, the response of the nonlinear damping oscillator is not like simple harmonic motion.

In general, after 10 s, the vibration velocity and amplitude of the nonlinear damping model $C_t = 80(V_t/V_{max})^{15}$ remain stable. The maximum vibration velocity of the nonlinear damping is 0.503 m/s which is higher than the velocity of the optimal constant damping oscillator (0.49 m/s), especially after 20 s. These findings demonstrate that the VIV responses of the nonlinear damping model $C_t = 80(V_t/V_{max})^{15}$ is stronger than the optimal constant damping model. The displacement also has a similar phenomenon (0.0708 m > 0.07 m). Considering the damping curve, high damping is adopted only at high velocity ($V_t/V_{max} > 0.7$), which helps to enhance the converted power. Therefore, the converted power of the nonlinear damping model is noticeably higher than the optimal constant damping (3.875 W > 3.626 W, 6.9% higher).

The velocity and vortex pattern around the oscillator with the nonlinear damping model (Convex Function Model) are presented in Fig. 17. Because of the high amplitude ($A = 0.0708$ m), the

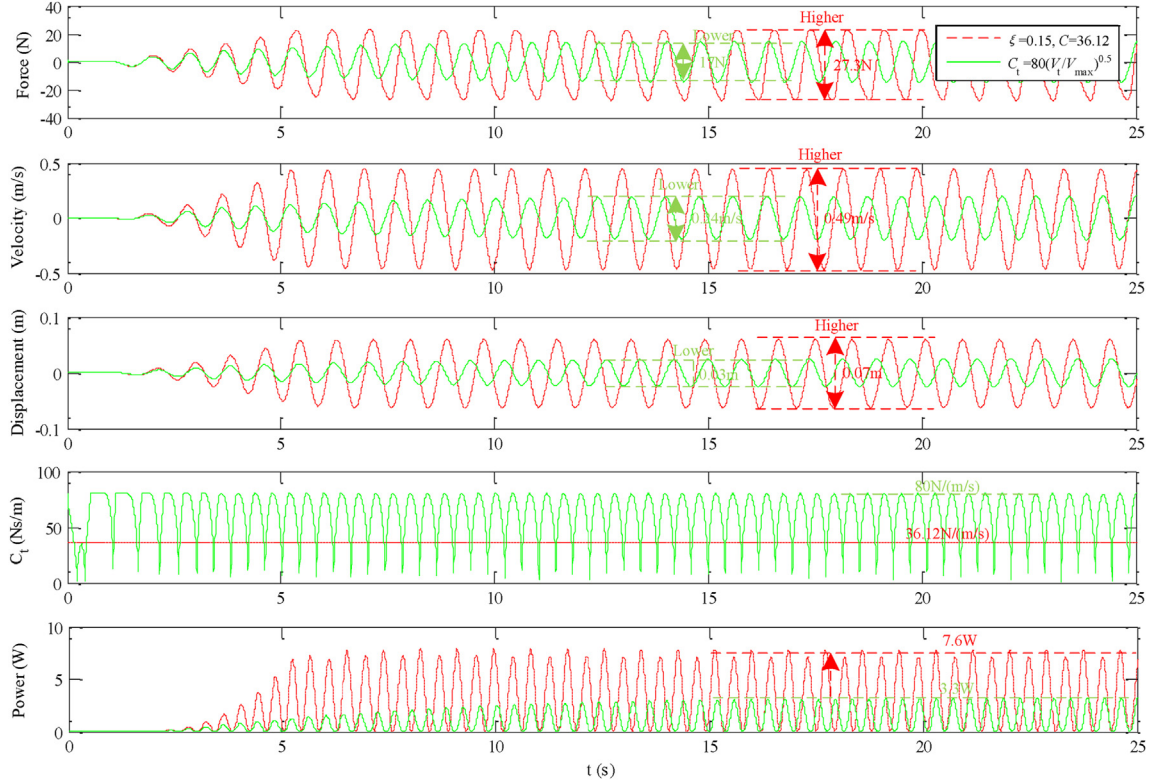


Fig. 13. Comparison of the fluid force, vibration velocity, displacement, damping, and converted power with the nonlinear damping model to the constant damping model.

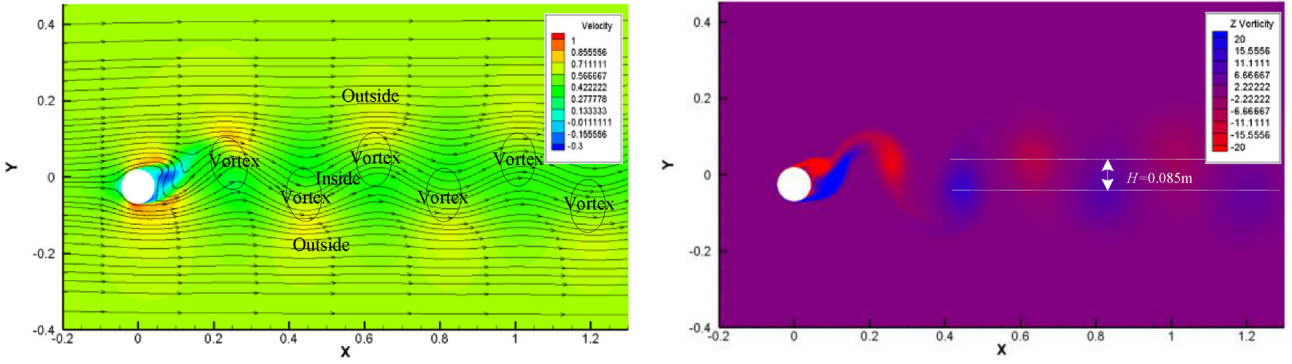


Fig. 14. Velocity distribution and Vortex pattern around the cylinder with the nonlinear damping $C_t = 80(V_t/V_{max})^{0.5}$ (Concave Function Model).

distance H between two rows of vortices increases to 0.23 m, which suggests the VIV response is stronger. Therefore, the flow structure is more complex and the velocity in the wake is much lower than that in the outside. However, the vortex structure is also 2S pattern, which is the same as the constant damping oscillator. 2P pattern is still not obvious due to relatively low amplitude.

4.4. Normalization and comparison of VIV responses with different damping models

Due to the difference of period and phase, it is difficult to compare the VIV responses. Normalization is the process of organizing data in post-processing. Therefore, the VIV responses, such as instantaneous velocity, damping and converted power are normalized and compared in Fig. 18. For the nonlinear damping model $C_t = 80(V_t/V_{max})^{15}$, the damping increases rapidly when at

high vibration velocity. The instantaneous velocity is higher than other models in most cases. High damping is adopted only when in the range of $0.13T_{\text{Onecycle}} \sim 0.34T_{\text{Onecycle}}$ and $0.63T_{\text{Onecycle}} \sim 0.84T_{\text{Onecycle}}$, as marked in Fig. 18. Otherwise, the instantaneous damping is close to 0. For the linear damping model $C_t = 60(V_t/V_{max})^{1.0}$ and nonlinear damping model $C_t = 80(V_t/V_{max})^{0.5}$, the instantaneous damping is relatively high in the whole cycle, but the converted power is relatively low.

The phase portraits of velocity-displacement are presented in Fig. 19 (a). It can be clearly found the blue line of the nonlinear damping model $C_t = 80(V_t/V_{max})^{15}$ is on the outermost side, which means when at the same vibration velocity, the displacement of the nonlinear damping model $C_t = 80(V_t/V_{max})^{15}$ is greater than other models. Also, when at the same vibration phase, the vibration velocity of the nonlinear damping model $C_t = 80(V_t/V_{max})^{15}$ is higher than other models.

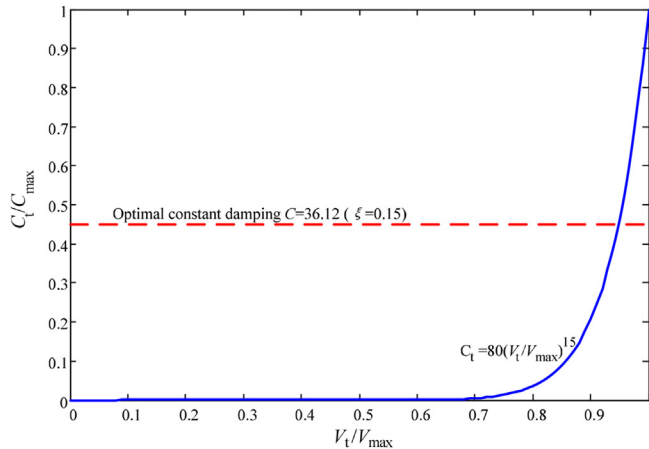


Fig. 15. Comparison between the constant damping model and nonlinear damping model $C_t = 80(V_t/V_{max})^{15}$ (Convex Function Model).

Furthermore, the phase portraits of power-velocity are compared in Fig. 19(b). For the optimal constant damping model $C = 36.12\text{N}/(\text{m/s})$, the maximum vibration velocity is less than 0.47 m/s , and the maximum power is less than 8W . For the linear damping model $C_t = 60(V_t/V_{max})^{1.0}$, the maximum vibration velocity is less than 0.37 m/s , and the maximum power is less than 8.5W . For the nonlinear damping model $C_t = 80(V_t/V_{max})^{15}$, when compared to the optimal constant damping model, the converted power is the highest. The maximum power is close to 20W . Besides, the maximum vibration velocity reaches up to 0.51 m/s , which is better than other models. If high load damping is adopted at low vibration velocity, the VIV responses will be suppressed in advance. It should be noted that as the exponent n increases, the shape of the

phase portraits of power-velocity gradually approach the shape of a basin. This shows that hydrokinetic energy will be extracted only when the vibration velocity is relatively high.

5. Results and discussion

5.1. Amplitude and frequency analysis

The VIV amplitude and frequency VS different model parameters (C_{max} and n) are compared in Fig. 20. The following observations can be made:

- (1) First, the effect of the maximum upper limit of damping C_{max} on the VIV amplitude is discussed. In general, when the exponent $n \leq 10$, reducing the maximum damping C_{max} directly promotes amplitude. For instance, when the exponent n is 6, the VIV amplitude increases from 0.043m ($A^*=0.48$) to 0.088m ($A^*=0.99$) with decreasing C_{max} (from 100 to 20). When $n > 10$, for the cases with $C_{max} = 20\text{N}/(\text{m/s})$, $C_{max} = 40\text{N}/(\text{m/s})$ and $C_{max} = 60\text{N}/(\text{m/s})$, this phenomenon is not obvious. Most notably, for $C_{max} = 40\text{N}/(\text{m/s})$, the amplitude curve crosses with the $C_{max} = 20\text{N}/(\text{m/s})$, which indicates that further reducing damping will not increase the VIV amplitude. Besides, when the exponent n is relatively high, the effect of C_{max} on the VIV amplitude is not significant.
- (2) Then, the effect of the exponent n is analyzed. Generally speaking, increasing n has a positive impact on the VIV response, especially when the maximum damping C_{max} is higher than $40\text{N}/(\text{m/s})$. More specially, when C_{max} is $60\text{N}/(\text{m/s})$, the VIV amplitude A increases from 0.0462m to 0.0812m with increasing n (from 0.5 to 20). When C_{max} is equal to $80\text{ N}/(\text{m/s})$, the VIV amplitude A increases from 0.0251m to 0.0758m . The reason is as the exponent n increases, the

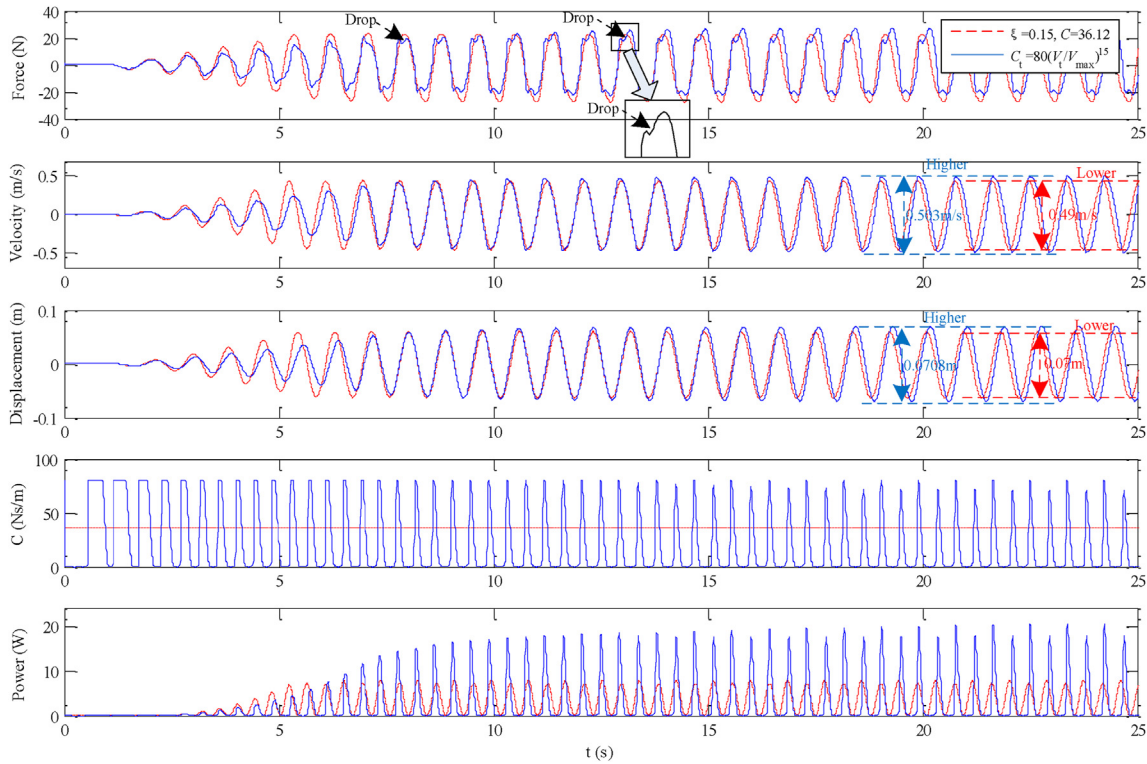


Fig. 16. Comparison of the fluid force, vibration velocity, displacement, damping, and converted power of with the nonlinear damping model to the constant damping model.

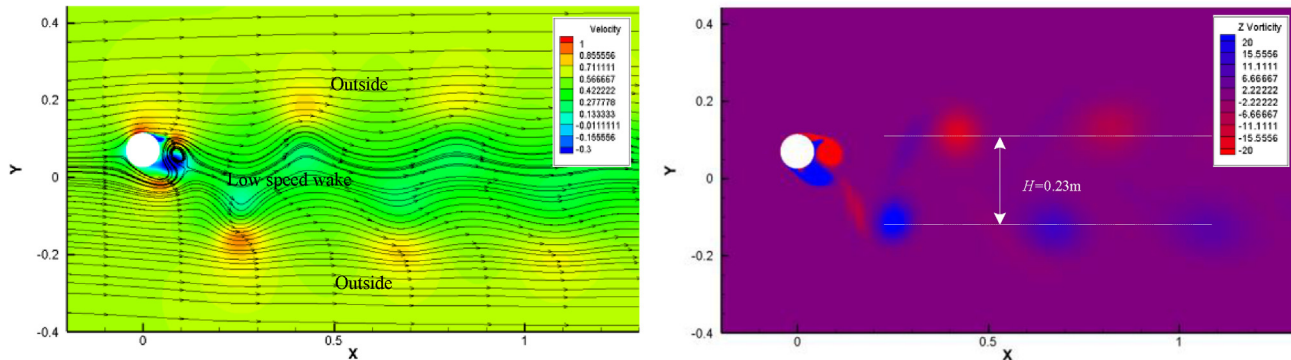


Fig. 17. Velocity distribution and Vortex pattern around the cylinder with the nonlinear damping $C_t = 80(U_t/U_{max})^{15}$ (Convex Function Model).

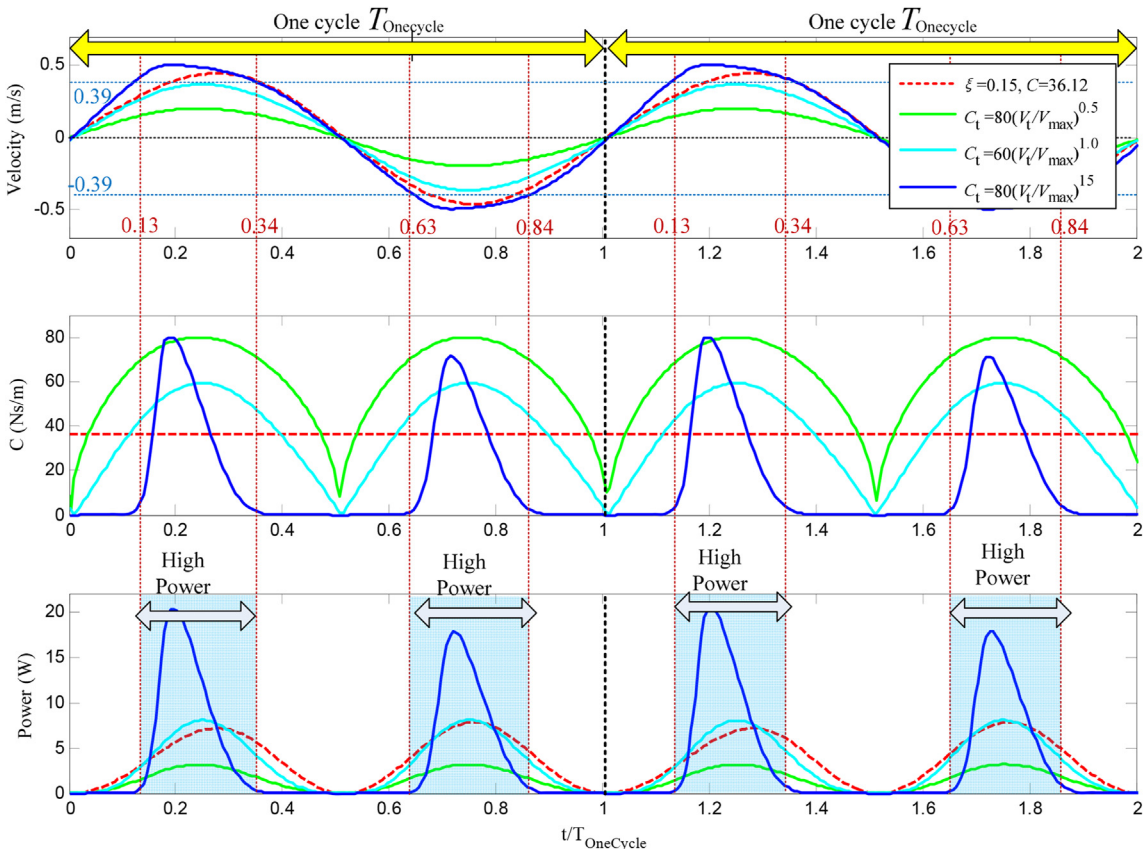


Fig. 18. Comparison of the time history of instantaneous velocity, damping and dynamic converted power with four different damping models.

- nonlinear damping model approaches a convex function, so the sensitivity of nonlinear damping is also enhanced at high vibration velocity. Consequently, it can be concluded that larger n is more suitable for the VIV response.
- (3) The VIV frequencies with different parameters (n and C_{max}) are compared in Fig. 20(b). In the VIV response, the frequency is close to the natural frequency of cylinder in water $f_{n,water} = (1/2\pi)\sqrt{K/M} = 1.12\text{Hz}$. For all cases, the frequency is about 1.1Hz–1.27Hz. The model parameters n and C_{max} affect the VIV amplitude and thereby affect the VIV frequency indirectly. Therefore, $f_{n,water}$ is not sensitive to the nonlinear damping model.

5.2. Energy transfer

The converted powers with different nonlinear damping models are compared in Fig. 21(a), which is the most important index in designing a VIV system. The power is closely related to the parameters (exponent n and maximum damping C_{max}) of the damping model. The energy transfer efficiencies are also compared in Fig. 21 (b). The following observations are made:

- (1) The converted power behaves differently at different region of the exponent n . When the exponent n is less than 6, the nonlinear damping model with $C_{max} = 60$ has the highest power. When the exponent n is higher than 6, the nonlinear damping model with $C_{max} = 80$ has the highest power.

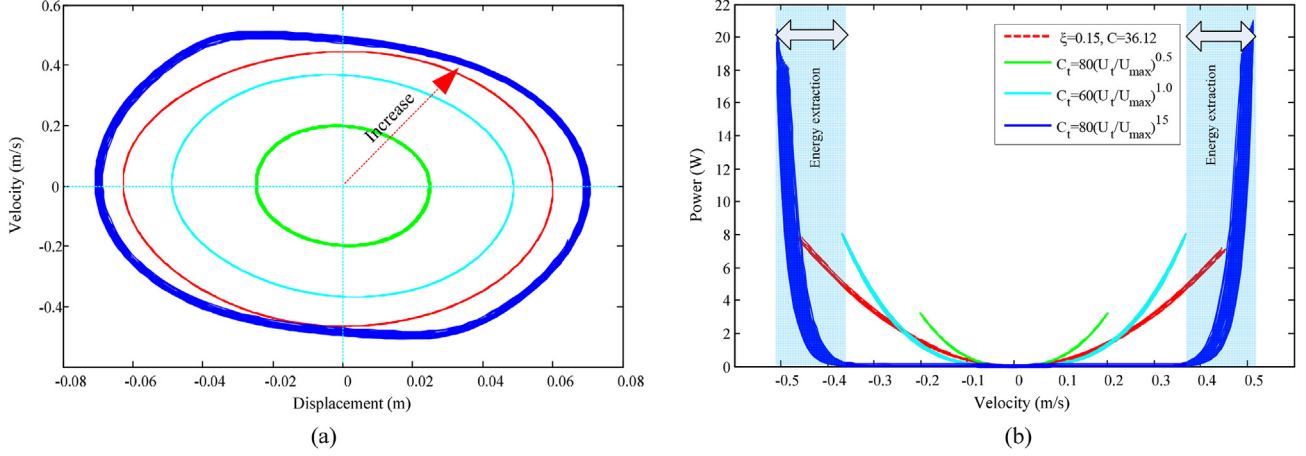


Fig. 19. Comparison of (a) Phase portraits of velocity-displacement and (b) Phase portraits of power-velocity with four different damping models.

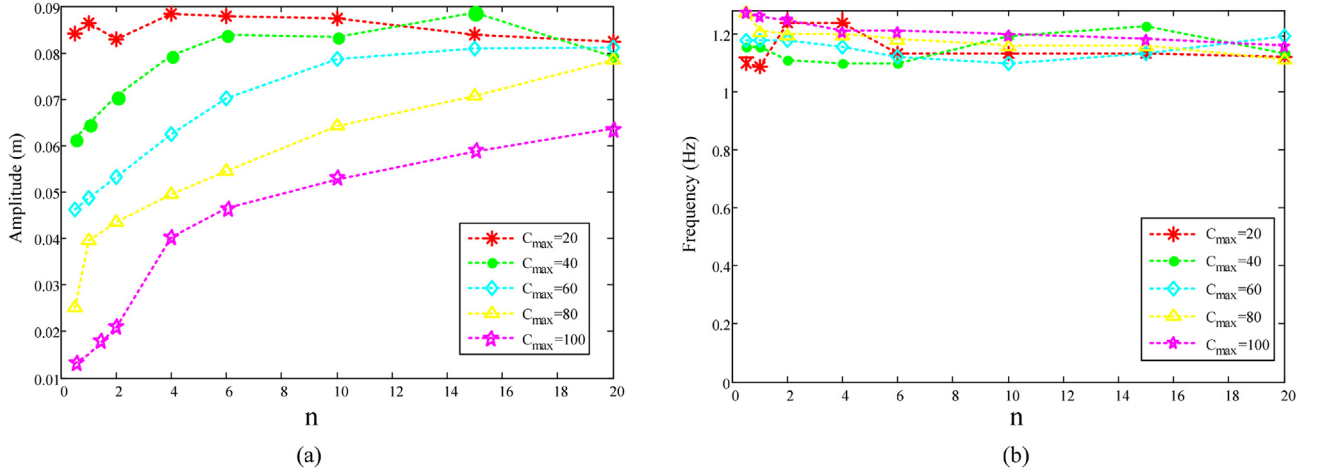


Fig. 20. Comparison of the VIV responses with different parameters (n and C_{max}) of the damping model: (a) VIV amplitude and (b) VIV frequency.

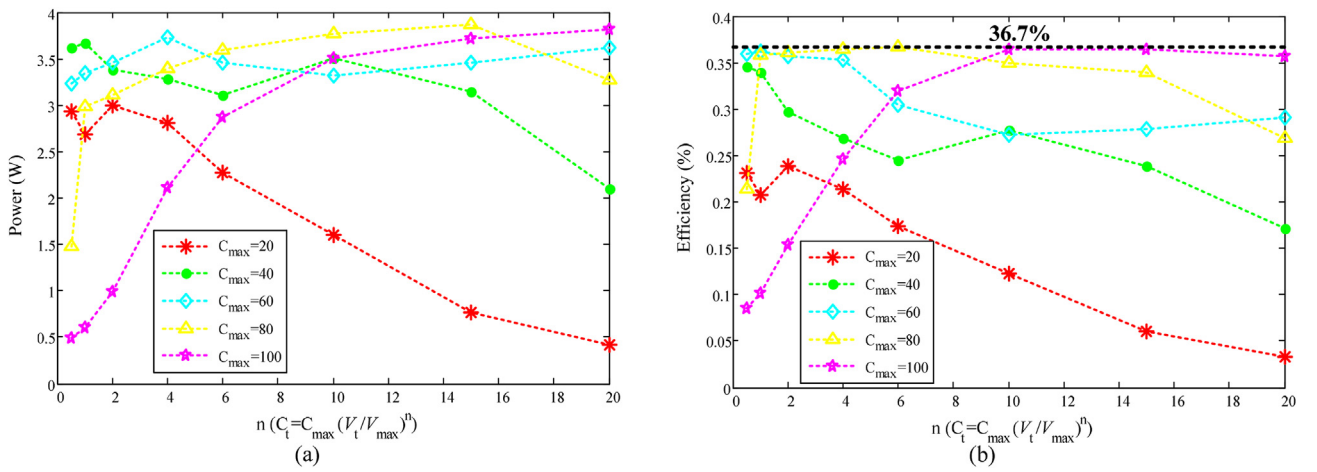


Fig. 21. Comparison of the VIV responses with different parameters (exponent n and maximum damping C_{max}) of the nonlinear damping model: (a) Converted power and (b) Energy transfer efficiency.

(2) The relationship between the power and model parameters (n and C_{max}) is nonlinear. When C_{max} is relatively low ($C_{max} = 20$ and 40), the converted power decrease with

increasing n . However, when C_{max} is relatively high ($C_{max} = 80$ and 100), the converted power increase with increasing n .

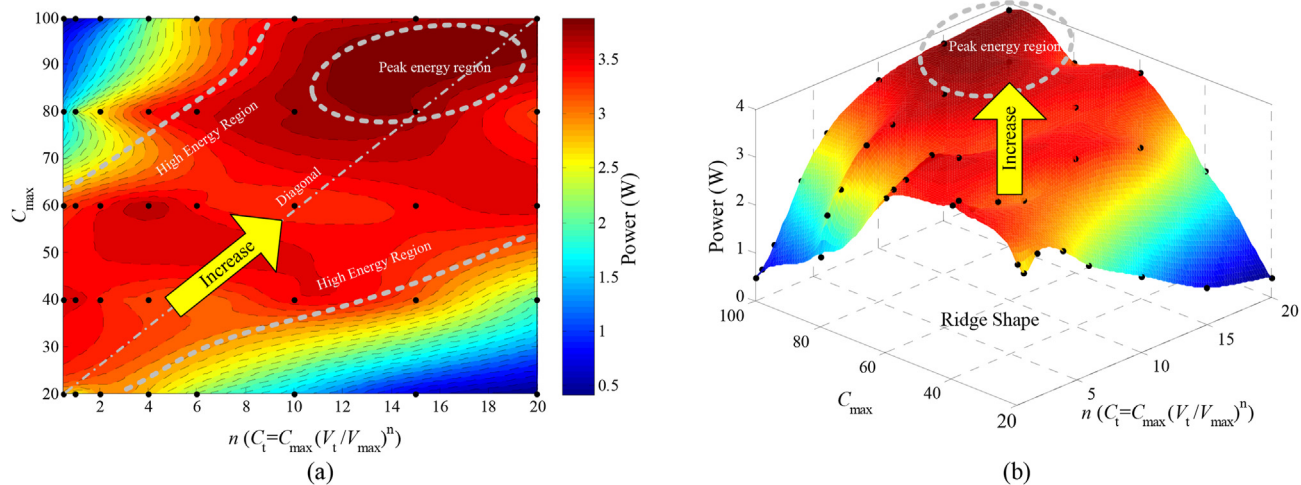


Fig. 22. Energy contour map and fitted response surface of the converted power.

- (3) Specifically, for different C_{max} , the maximum converted power at flow velocity $U = 0.55$ m/s ($U^* \approx 6$) is 3.0W ($C_{max} = 20$, $n = 2$), 3.67W ($C_{max} = 40$, $n = 1$), 3.73W ($C_{max} = 60$, $n = 4$), 3.87W ($C_{max} = 80$, $n = 15$), and 3.82W ($C_{max} = 100$, $n = 20$), respectively. Clearly, the maximum converted power is higher than the power of the optimal constant damping (3.875W > 3.626W, 6.9% higher).
- (4) According to Eqs. (5) and (6) presented in Section 3.1, the VIV energy transfer efficiency η_{VIV} can be calculated by $\eta_{VIV} = P_{VIV}/(P_{fluid} \times \text{Betz Limit}) \times 100\%$, the efficiency depends primarily on the power and VIV amplitude. Therefore, the curves of the energy transfer efficiency (Fig. 21(b)) are similar with that of the converted power (Fig. 21(a)).
- (5) For different C_{max} , the maximum energy transfer efficiency is 23.8% ($C_{max} = 20$, $n = 2$), 34.5% ($C_{max} = 40$, $n = 0.5$), 36.3% ($C_{max} = 60$, $n = 1$), 36.7% ($C_{max} = 80$, $n = 6$), and 36.5% ($C_{max} = 100$, $n = 10$), respectively. It is noteworthy that the maximum energy transfer efficiencies plateau at about 36.7%, which indicates there is an upper limit for the optimization of the nonlinear damping scheme.

Fig. 22(b) presents the energy contour map and fitted response surface of the converted power to better illustrate the effect of the model parameters. In the energy distribution map, “high energy region” and “peak energy region” are marked separately. The high energy region is located on both sides of the diagonal, which looks like a ridge. The peak energy region is in the top right-hand corner ($80 < C_{max} < 100$, $10 < n < 20$). It is also concluded that the converted power increases with the growth of the two model parameters (n and C_{max}).

6. Conclusions

In this study, the effects of nonlinear damping on VIV hydrokinetic energy transfer are numerically investigated. The VIV responses are simulated and analyzed using Fluent and UDF module in which the developed algorithms for the motion equation and nonlinear damping model are embedded. Different damping models including constant damping model, linear damping model and nonlinear damping model are discussed in detail. The main conclusions can be drawn:

- (1) The nonlinear damping scheme is put forward based on the idea of adjusting the damping dynamically with the vibration velocity. The main conclusion is the nonlinear damping produces the highest power.
- (2) For the convex function nonlinear damping model, the sensitivity is very high when the vibration velocity approaches the maximum vibration velocity. When the vibration velocity is relatively low, the damping is close to zero and remains stable.
- (3) The relationship between the power and model parameters (n and C_{max}) is nonlinear. When C_{max} is relatively high, the converted power increases with the exponent n . However, when C_{max} is relatively low, the power decreases with the exponent n .
- (4) The nonlinear damping is especially effective for enhancing the VIV responses. When compared to the optimal constant damping, the power of the optimal nonlinear damping ($C_t = 80(V_t/V_{max})^{15}$) increases by 6.9%.
- (5) In addition, in the optimal nonlinear damping model $C_t = 80(V_t/V_{max})^{15}$, although the peak value of damping is increased, the vibration velocity and amplitude are not significantly suppressed due to the dynamic change of the nonlinear damping.
- (6) The nonlinear relationship between the converted power and model parameters (C_{max} and n) is revealed. The fitted response surface of the power is shaped like a ridge. The converted power increases with the common growth of two parameters (n and C_{max}).

CRediT authorship contribution statement

Baoshou Zhang: Investigation, Writing – original draft, preparation, Revising. **Boyang Li:** Data curation, Revising. **Song Fu:** Conceptualization. **Zhaoyong Mao:** Conceptualization, Methodology. **Wenjun Ding:** Visualization, Writing – review & editing.

Declaration of competing interest

The authors declare that they have no known competing financial interests or personal relationships that could have appeared to influence the work reported in this paper.

Acknowledgement

Project funded by Tsinghua University Shumu Scholar Program (2020SM027) and China Postdoctoral Science Foundation (BX20200187, 2021M691718, 2021M692616).

References

- [1] P.W. Bearman, Vortex shedding from oscillating bluff bodies, *Annu. Rev. Fluid Mech.* 16 (1) (1984) 195–222.
- [2] A. Khalak, C.H. Williamson, Motions, forces and mode transitions in vortex-induced vibrations at low mass-damping, *J. Fluid Struct.* 13 (7–8) (1999) 813–851.
- [3] C.H. Williamson, R. Govardhan, Vortex-induced vibrations, *Annu. Rev. Fluid Mech.* 36 (2004) 413–455.
- [4] J.H. Lee, N. Xiros, M.M. Bernitsas, Virtual damper–spring system for VIV experiments and hydrokinetic energy conversion, *Ocean Eng.* 38 (5–6) (2011) 732–747.
- [5] J.T. Klamo, The application of controlled variable magnetic eddy current damping to the study of vortex-induced vibrations, *Exp. Fluid* 47 (2) (2009) 357–367.
- [6] W. Wu, M.M. Bernitsas, K. Maki, RANS simulation versus experiments of flow induced motion of circular cylinder with passive turbulence control at $35,000 < Re < 130,000$, *J. Offshore Mech. Arctic Eng.* 136 (4) (2014).
- [7] P.W. Bearman, Circular cylinder wakes and vortex-induced vibrations, *J. Fluid Struct.* 27 (5–6) (2011) 648–658.
- [8] S. Rashidi, M. Hayatdavoodi, J.A. Esfahani, Vortex shedding suppression and wake control: a review, *Ocean Eng.* 126 (2016) 57–80.
- [9] M.R. Arif, N. Hasan, Vortex shedding suppression in mixed convective flow past a square cylinder subjected to large-scale heating using a non-Boussinesq model, *Phys. Fluids* 31 (2) (2019), 023602.
- [10] W. Wang, B. Song, Z. Mao, W. Tian, T. Zhang, Numerical investigation on VIV suppression of the cylinder with the bionic surface inspired by giant cactus, *Ocean Eng.* 214 (2020), 107775.
- [11] W. Xu, C. Ji, H. Sun, W. Ding, M.M. Bernitsas, Flow-induced vibration of two elastically mounted tandem cylinders in cross-flow at subcritical Reynolds numbers, *Ocean Eng.* 173 (2019) 375–387.
- [12] W. Chen, C. Ji, D. Xu, Z. Zhang, Vortex-induced vibrations of two inline circular cylinders in proximity to a stationary wall, *J. Fluid Struct.* 94 (2020), 102958.
- [13] A.B. Rostami, M. Armandei, Renewable energy harvesting by vortex-induced motions: review and benchmarking of technologies, *Renew. Sustain. Energy Rev.* 70 (2017) 193–214.
- [14] M.M. Bernitsas, K. Raghavan, Y. Ben-Simon, E.M.H. Garcia, VIVACE (Vortex Induced Vibration Aquatic Clean Energy): A New Concept in Generation of Clean and Renewable Energy from Fluid Flow, 2008.
- [15] M.M. Bernitsas, Y. Ben-Simon, K. Raghavan, E.M.H. Garcia, The VIVACE converter: model tests at high damping and Reynolds number around 105, *J. Offshore Mech. Arctic Eng.* 131 (1) (2009).
- [16] B. Zhang, B. Song, Z. Mao, W. Tian, B. Li, Numerical investigation on VIV energy harvesting of bluff bodies with different cross sections in tandem arrangement, *Energy* 133 (2017) 723–736.
- [17] B. Zhang, Z. Mao, L. Wang, S. Fu, W. Ding, A novel V-shaped layout method for VIV hydrokinetic energy converters inspired by geese flying in a V-Formation, *Energy* 230 (2021), 120811.
- [18] B. Zhang, B. Song, B. Li, L. Su, W. Ding, Numerical study of the effect of submergence depth on hydrokinetic energy conversion of an elastically mounted square cylinder in FIV, *Ocean Eng.* 200 (2020), 107030.
- [19] M.M. Bernitsas, Harvesting energy by flow induced motions, in: Springer Handbook of Ocean Engineering, Springer, Cham, 2016, pp. 1163–1244.
- [20] E.S. Kim, M.M. Bernitsas, R. Ajith Kumar, Multicylinder flow-induced motions: enhancement by passive turbulence control at $28,000 < Re < 120,000$, *J. Offshore Mech. Arctic Eng.* 135 (2) (2013).
- [21] O. Kemal Kinaci, S. Lakka, H. Sun, E. Fassezke, M.M. Bernitsas, Computational and experimental assessment of turbulence stimulation on flow induced motion of a circular cylinder, *J. Offshore Mech. Arctic Eng.* 138 (4) (2016).
- [22] H. Park, E.S. Kim, M.M. Bernitsas, Sensitivity to zone covering of the map of passive turbulence control to flow-induced motions for a circular cylinder at $30,000 \leq Re \leq 120,000$, *J. Offshore Mech. Arctic Eng.* 139 (2) (2017).
- [23] L. Ding, L. Zhang, M.M. Bernitsas, C.C. Chang, Numerical simulation and experimental validation for energy harvesting of single-cylinder VIVACE converter with passive turbulence control, *Renew. Energy* 85 (2016) 1246–1259.
- [24] W. Ding, H. Sun, W. Xu, M.M. Bernitsas, Numerical investigation on interactive FIO of two-tandem cylinders for hydrokinetic energy harnessing, *Ocean Eng.* 187 (2019), 106215.
- [25] W. Yuan, H. Sun, H. Li, M.M. Bernitsas, Flow-induced oscillation patterns for two tandem cylinders with turbulence stimulation and variable stiffness and damping, *Ocean Eng.* 218 (2020), 108237.
- [26] H. Sun, E.S. Kim, G. Nowakowski, E. Mauer, M.M. Bernitsas, Effect of mass-ratio, damping, and stiffness on optimal hydrokinetic energy conversion of a single, rough cylinder in flow induced motions, *Renew. Energy* 99 (2016) 936–959.
- [27] H. Sun, C. Ma, M.M. Bernitsas, Hydrokinetic power conversion using Flow Induced Vibrations with nonlinear (adaptive piecewise-linear) springs, *Energy* 143 (2018) 1085–1106.
- [28] J. Wang, S. Sun, L. Tang, G. Hu, J. Liang, On the use of metasurface for Vortex-Induced vibration suppression or energy harvesting, *Energy Convers. Manag.* 235 (2021), 113991.
- [29] J. Wang, S. Sun, G. Hu, Y. Yang, L. Tang, P. Li, G. Zhang, Exploring the potential benefits of using metasurface for galloping energy harvesting, *Energy Convers. Manag.* 243 (2021), 114414.
- [30] H. Zhu, T. Tang, T. Zhou, M. Cai, O. Gaidai, J. Wang, High performance energy harvesting from flow-induced vibrations in trapezoidal oscillators, *Energy* (2021), 121484.
- [31] B. Zhang, K.H. Wang, B. Song, Z. Mao, W. Tian, Numerical investigation on the effect of the cross-sectional aspect ratio of a rectangular cylinder in FIM on hydrokinetic energy conversion, *Energy* 165 (2018) 949–964.
- [32] B. Zhang, B. Song, Z. Mao, B. Li, M. Gu, Hydrokinetic energy harnessing by spring-mounted oscillators in FIM with different cross sections: from triangle to circle, *Energy* 189 (2019), 116249.
- [33] A. Mehmood, A. Abdelkefi, M.R. Hajj, A.H. Nayfeh, I. Akhtar, A.O. Nuhait, Piezoelectric energy harvesting from vortex-induced vibrations of circular cylinder, *J. Sound Vib.* 332 (19) (2013) 4656–4667.
- [34] K. Raghavan, M.M. Bernitsas, Enhancement of high damping VIV through roughness distribution for energy harvesting at $8 \times 10^3 < Re < 1.5 \times 10^5$, *Int. Conf. Offshore Mech. Arctic Eng.* 48234 (2008, January) 871–882.
- [35] A.K. Soti, J. Zhao, M.C. Thompson, J. Sheridan, R. Bhardwaj, Damping effects on vortex-induced vibration of a circular cylinder and implications for power extraction, *J. Fluid Struct.* 81 (2018) 289–308.
- [36] A.K. Soti, M.C. Thompson, J. Sheridan, R. Bhardwaj, Harnessing electrical power from vortex-induced vibration of a circular cylinder, *J. Fluid Struct.* 70 (2017) 360–373.
- [37] J.H. Lee, M.M. Bernitsas, High-damping, high-Reynolds VIV tests for energy harvesting using the VIVACE converter, *Ocean Eng.* 38 (16) (2011) 1697–1712.
- [38] H. Sun, C. Ma, E.S. Kim, G. Nowakowski, E. Mauer, M.M. Bernitsas, Hydrokinetic energy conversion by two rough tandem-cylinders in flow induced motions: effect of spacing and stiffness, *Renew. Energy* 107 (2017) 61–80.
- [39] S. Li, J. Xu, X. Pu, T. Tao, H. Gao, X. Mei, Energy-harvesting variable/constant damping suspension system with motor based electromagnetic damper, *Energy* 189 (2019), 116199.
- [40] H. Sun, M.M. Bernitsas, Bio-inspired adaptive damping in hydrokinetic energy harnessing using flow-induced oscillations, *Energy* 176 (JUN.1) (2019) 940–960.
- [41] C. Ma, H. Sun, G. Nowakowski, E. Mauer, M.M. Bernitsas, Nonlinear piecewise restoring force in hydrokinetic power conversion using flow induced motions of single cylinder, *Ocean Eng.* 128 (2016) 1–12.
- [42] N. Jauvtis, C.H.K. Williamson, The effect of two degrees of freedom on vortex-induced vibration at low mass and damping, *J. Fluid Mech.* 509 (2004) 23–62.
- [43] Z. Kang, C. Cheng, G. Ma, A numerical investigation of the effects of Reynolds number on vortex-induced vibration of the cylinders with different mass ratios and frequency ratios, *Int. J. Nav. Arch. Ocean.* 11 (2) (2019) 835–850.
- [44] W. Wang, Z.Y. Mao, B.W. Song, P. Han, Numerical investigation on vortex-induced vibration suppression of the cactus-inspired cylinder with some ribs, *Phys. Fluids* 33 (2021), 037127.